Capping the electronic lone pair of the As(III) central atom in the Keggin-type anion. From experimental - theoretical interplay to evidence

Fa Ibrahima Bamba,[a] Clément Falaise,[a] Nathalie Leclerc,[a] Mohamed Haouas,[a] Gildas Gbassi,[b] Patrick Atheba,[c] Mathieu Fregnaux,[a] Jordi Buils,[d,e] Mireia Segado-Centellas,[e] Carles Bo*[d] and Emmanuel Cadot*[a]*

KEYWORDS. Polyoxometalate, Vanadium, Inorganic Synthesis, NMR,

ABSTRACT: Stereochemistry of the polycondensation processes within the Keggin-type derivatives is mainly governed by the nature of the assembling group X, being either tetrahedral or trigonal. While arrangements containing a tetrahedral group such as $\{PO_4\}$, $\{SiO_4\}$ or $\{BO_4\}$ correspond mostly to the usual $\{XM_{12}\}$ Keggin structure, those built on trigonal unit $\{AsO_3\}$, $\{SbO_3\}$ or $\{BiO_3\}$ give rise to open molecular structures resulting from connections of $\{XM_9\}$ subunits through metal-oxo cationic fragments. Such a difference is due to the presence of the electronic lone pair carried by the central X(III) atom which usually prevents the metal-oxo shell from closing which should lead to the restauration of the Keggin-type arrangement. Nevertheless, we show here an unusual behavior during the condensation of the vanadate VO_3^- under almost stoichiometric conditions onto the B-type isomer α-$[AsW_9O_{33}]^{9-}$ that led to the mixed-metal

Keggin derivative α-$[AsW_9V_3O_{39}]^{6-}$ in which the arsenic atom has retained its initial +III oxidation state. Experimental evidences were provided by multinuclear NMR characterization, including ^{51}V, ^{183}W and ^{17}O NMR, supported by XPS analysis revealing unambiguously the fingerprints of the As(III) atoms compared to those of the As(V). Moreover, such a striking structural feature is fully consistent with the versatile coordination of the V(V) atoms which makes it possible for the μ_3-O bridging oxygen of the $\{V_3\}$ cap to be absent in front of the electronic lone pair of the As(III) ion. In addition, DFT studies give consistency to the electronic structure of this new Keggin-type derivative. At last, structural, spectroscopic and electrochemical properties of this new version of the Keggin structure were compared to other archetypal vanadium-containing anions and then discussed with regard to the geometry and vicinity of the vanadium atoms.

INTRODUCTION

Polyoxometalates (POMs) represent a remarkable class of polynuclear metal oxide anions built from early transition metal cations like V^V, Mo^{VI} or W^{VI}.[1,2] However, POM assemblies can include almost all the chemical elements in their metal-oxo framework that results of an extremely wide chemical composition associated to high structural diversity.[3] Actually, one of the most striking properties of POM compounds is surely their ability to exchange electrons reversibly and massively without significant structural change,[4,5] making them promising electro-active components for numerous applications in various domains in relationship with electrochemical energy conversion or storage.[6,7]

However, these promising applications are linked to their intrinsic mixed-valence fundamental electronic properties, which essentially fall into three classes according to Robin & Day's classification.[8] Then, depending on the structure, composition or medium, various behaviors can be observed for the transferred *d* electrons such as i) strongly

localized (class I), thermally / optically delocalized (class II) or fully delocalized within metal-centered orbitals (class III). In context, these properties give rise to many potential and specific applications where polyoxometalates are interfaced with various materials such as carbon,[9,10] nitride[11] or sulphide[12] based nanomaterials. Furthermore, the incorporation of transition metals into POM framework corresponds to a practical and simple method for the design of robust mixed metal molecular electrocatalysts, which operate from a fine electronic interplay between the transition metal catalytic site and the redox active POM units.[13] Then, such an approach has demonstrated to be fruitful to develop relevant POM-based electrocatalysts, efficient for different reactions such as proton,[14,15] CO_2,[16] O_2 or N_2 reduction[17,18] as well water oxidation[19,20] or biomass conversion.[21] Another promising application for POM-based systems is their use as active components in redox flow batteries. In particular, vanadium-containing POMs exhibit high redox potentials centered on the V^V/V^{IV} couple with values between ~ 0.5 and ~ 0.8 V *vs*. *NHE*, making them good candidate for catholyte matrices.[22] Nevertheless, the redox properties of the V centers depend in part on the structural environment of the $\{VO_x\}$ polyhedra.[23] As an illustrative example, the redox potential of the V center in the monosubstituted Dawson-type anion $[P_2W_{17}VO_{62}]^{7-}$ is modified by about 60 mV when the location of the V atom changes from the polar (α_2 isomer) to the equatorial position (α_1 isomer) within the POM framework.[24] Herein, we report on the first Keggin-type anion which exhibits a triad of pure square pyramidal vanadium (V) capping the trivacant B-$[AsW_9O_{33}]^{9-}$ subunit. We provide ample evidence of such a molecular organization using diverse and complementary analytical methods such as X-ray diffraction, ^{51}V, ^{183}W and ^{17}O NMR, XPS, electrochemistry and theoretical calculations, all of which are consistent with or confirm the presence of the central trigonal $\{AsO_3\}$ group in close contact with the

{V_3O_6} cap in line with the structural hypothesis. In this study, the physicochemical consequences of oxygen-deficiency of the Keggin framework have been evaluated by comparing spectroscopic and electrochemical properties with other archetypical vanadium substituted polyoxotungstates such as the Keggin-type trisubstituted α-(1,2,3)-$[AsW_9V_3O_{40}]^{6-}$ or the sandwich-type α-B-$[AsW_9O_{33})_2(VO)_3]^{9-}$ anions, where vanadium centres exhibit an octahedral or square pyramidal environment, respectively.

Figure 1. Schematic view of the formal restauration of the Keggin-type structure from the B-type α-$[AsW_9O_{33}]^{9-}$ by the addition of a fourth triad {M_3O_6} containing a missing μ_3-Oa oxygen atom.

RESULTS AND DISCUSSION

Synthesis. The development of polyoxotungstate chemistry has mapped comprehensive

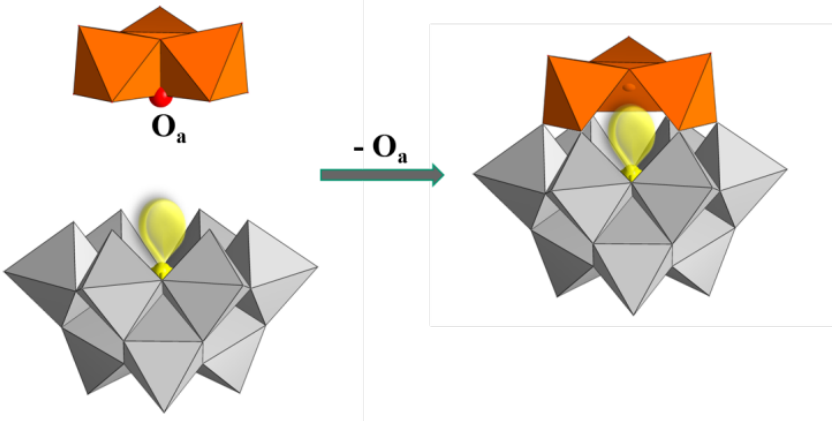

interconversion schemes that make possible the design of mixed metal compounds using rational protocols, where stereospecific acidic condensation and basic hydrolysis processes alternate in multistep strategies.[25] For example, such a synthetic methodology has proven to be highly relevant for the synthesis of Mo-V-W Dawson type anions, allowing the isolation of more than 20 derivatives, differing in their Mo/V/W composition and the location of the metallic centers that gives rise to numerous positional isomers.[26,27] A similar methodology can be also applied to the polyoxotungstates deriving from the Keggin series. While successive addition of metalate ions on the A-type trivacant anions α-A-$[PW_9O_{34}]^{9-}$

or α-A-$[SiW_9O_{34}]^{10-}$ can restore the saturated Keggin-type anions α-(1,2,3)-$[XW_9M_3O_{40}]^{n-}$, the use of the B-type isomers α-B-$[XW_9O_{33}]^{9-}$ with X = As^{III}, Sb^{III} or Bi^{III} in comparable conditions gives modular species such as dimeric or macrocyclic arrangements.[28,29,30,31] This stereochemical difference arises from the presence of the trigonal assembling group $\{XO_3\}$, whose the electronic lone pair is expected to induce unfavorable electrostatic and steric repulsions with the μ_3-oxygen atom (O_a-type) of the $\{M_3O_7\}$ capping groups. (see Figure 1). Then, the stereochemistry of the B-type α-$[XW_9O_{33}]^{9-}$ is mostly known to produce sandwich-type compounds or large modular species resulting from connection of the B-$[AsW_9O_{33}]^{9-}$ moiety through cationic metallic units.[30,29] Actually, the restauration of the Keggin structure from the B-type anion might be possible in the case where the μ_3-O_a is absent, which means that the three metallic centers of the capping triad would adopt a square-pyramidal environment. Such a situation remains rare with tungsten (VI) or molybdenum (VI), but frequently observed with metal centres exhibiting lower oxidation state.[32,33] In the case of vanadium (V), both situations are encountered depending on the steric environment of the coordination sphere of the vanadium atom.[34] Thus, condensation of vanadate ions $[VO_3]^-$ on the trivacant species $[AsW_9O_{33}]^{9-}$ has been investigated by

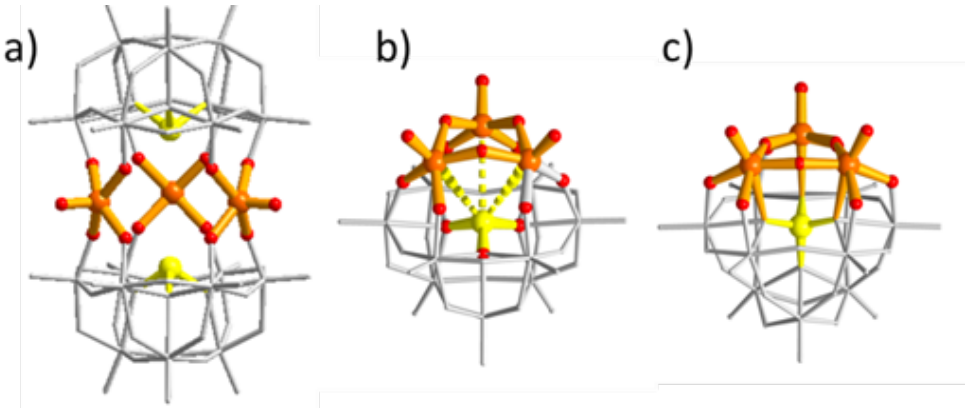

Figure 2. Structural representations highlighting different arrangements of the vanadium centres, including the square-based pyramidal within a) the sandwich-type compound α-B-$[AsW_9O_{33})_2(VO)_3]^{9-}$ and in b) the α-(1,4,9)-$[AsW_9V_3O_{39}]^{6-}$ or octahedral in c) the α-(1,2,3)-$[AsW_9V_3O_{40}]^{6-}$ (c); color code : orange spheres and sticks = vanadium atoms and V-O bonds, yellow spheres and sticks = arsenic atoms and As-O bonds, grey sticks = W-O frameworks.

using ^{51}V NMR. For ratio V/{AsW_9} ~ 3, ^{51}V NMR analysis reveals the presence of two predominant species observed at –509 ppm and –544 ppm which have been attributed to the Lindqvist anion[35] cis-$[V_2W_4O_{19}]^{4-}$ and to the targeted species α-(1,4,9)-$[AsW_9V_3O_{39}]^{6-}$, respectively. Actually, balance between both species is sensitive to the *p*H. Whereas at *p*H~ 1, the formation of the Lindqvist derivative is favored, in acetate buffer (*p*H = 4.8), the condensation reaction results mainly in the formation of the Keggin-type anion α-(1,4,9)-$[AsW_9V_3O_{39}]^{6-}$ as the predominant species. Applying precipitation and crystallization usual procedures allow to get K_6[α-(1,4,9)-$AsW_9V_3O_{39}$]•$14H_2O$ with a purity close to 100%. Moreover, the conventional trivanadium substituted K_6[α-(1,2,3)-$AsW_9V_3O_{40}$]•$22H_2O$ anion has been prepared from the A-type trivacant anion α-A-$[AsW_9O_{34}]^{9-}$ using procedure adapted from literature[36,25] (see ESI, section S3 for synthesis details). Furthermore, the numbering of the positions of the three vanadium atoms in the Keggin-type arrangement follows the IUPAC recommendations (for details, see ESI, section S2),[37] and a selection of

arrangements resulting from condensation of vanadate on the A- or B-type trivacant {AsW_9} are depicted in Figure 2.

Structural analysis

The potassium salt $K_6[\alpha\text{-}(1,4,9)\text{-}AsW_9V_3O_{39}]\bullet 14H_2O$ gave suitable crystals for single-crystal X-ray diffraction analysis. Structure refinement has been carried out using tetragonal system in the $P\bar{4}3m$ space group (see ESI, Section S4 for further details). The structure analysis reveals the presence of a Keggin-type anion in the cubic crystallographic cell in which, the three vanadium and the nine tungsten atoms were not distinguishable among the location of the twelve metallic positions. Such a situation, shown in Figure 3a is fairly consistent with a statistical disorder of the anion over its crystallographic position that results of twelve equivalent metallic positions occupy statistically by 25% of vanadium atom and by 75% of tungsten atom. Furthermore, such a disorder generates a quite perfect central tetrahedron which arises from the equal distribution of the central {AsO_3} group over the four equivalent positions of the tetrahedron. According to this disorder scheme, the three O_a-type oxygen atoms have been refined with a statistical occupancy factor of 75% over four tetrahedral positions. Then, despite the disorder which precludes the location of the V and W atoms, the important result of this study lies in the evidence that condensation of vanadate ions onto the B-type trivacant anion α-B-$[AsW_9O_{33}]^{9-}$ is able to restore the Keggin type anions. Then, the structural analysis revealed bond lengths and angle parameters, which lie in the usual range found for the archetypical Keggin type structure, such as the $[\alpha\text{-}GaW_{12}O_{40}]^{5-}$ anion, in which the central atom Ga(III) belong to the same period of that of As(III) atom (see ESI, Section S5, Table S2 for structural details).[38] Nevertheless, assuming that the central arsenic ion retains the As(III) oxidation

state by carrying the electronic lone pair in the trigonal geometry, the environment of the three vanadium atoms in the metal-oxo shell of the Keggin-type framework remains questioning.

Computational studies have therefore been performed to circumvent the disorder situation by optimizing a geometry that consists of a α-B-{AsW_9O_{33}} subunit capped by three square-pyramidal vanadium atoms forming a triad (see Figure 3b). The calculated structure has been established in the C_{3v} symmetry and orbital energies and Gibbs free energies indicate that such a structural arrangement should exhibit similar stability to the conventional anion α-(1,2,3)-$[AsW_9V_3O_{40}]^{6-}$. In the structure, the three square-pyramidal vanadium centers are equally separated by a distance of 3.324 Å from the As atom, while the calculated V=O bond distances exhibit an usual value of 1.624 Å. Besides, the W=O bond lengths remain significantly longer (1.744 Å).

These computed geometrical parameters have been compared to those obtained from the conventional Keggin type anion α-(1,4,9)-$[AsW_9V_3O_{40}]^{6-}$ or from the sandwich-type compound α-B-$[AsW_9O_{33})_2(VO)_3]^{9-}$ highlighting slight but significant variations of the V=O bond length in relationship with the specific situation of the vanadium atoms (see ESI, Section S5, Table S2). Then, the shortest V=O distance (1.589 (9) Å) however, is observed in the sandwich-type anion, where the V center retains a pure square-pyramidal arrangement.[34] The longest V=O distance is however observed in the conventional Keggin ion α-$[AsW_9V_3O_{40}]^{6-}$ in which the vanadium centers maintain a classical octahedral geometrical environment by interacting with a μ_3-O_a located in trans to the V=O bond. Despite the long O_a•••V distance of 2.455 Å, the trans-influence is manifested by a slight increase in the V=O bond of 1.626 Å. At last, in the B-type Keggin anion, the vanadium atoms adopt an intermediate situation with a V=O bond distance of 1.624 Å which could

be the fingerprint of the trans-influence arising from the interaction between the electronic lone pair of the As atom and the V metal centers (see Figure 3b).

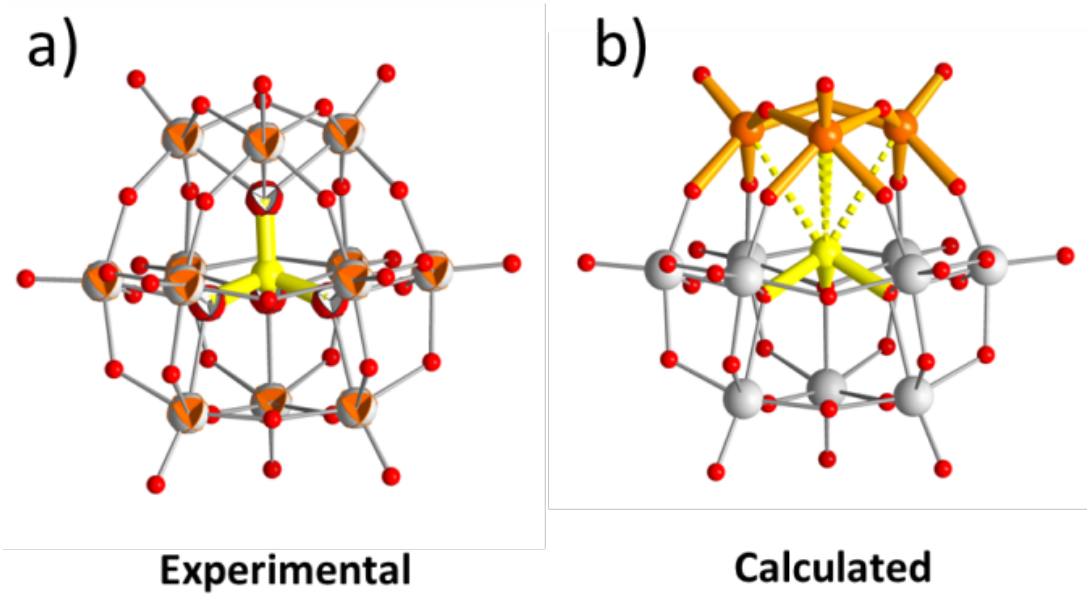

Figure 3. Ball & stick representations of the α-(1,4,9)-$[AsW_9V_3O_{39}]^{6-}$ anion. a) Experimental X-ray diffraction analysis showing a disordered situation where the $\{V_3\}$, $\{W_3\}$ triads and the $\{AsO_3\}$ trigonal group are distributed statistically over the four tetrahedral positions; b) calculated structure showing the trivanadium cap closing the $\{AsW_9O_{33}\}$ unit and interacting with the electronic lone pair carried by the central As(III) atom. Color code: orange sphere = vanadium, grey sphere = tungsten, red = oxygen; yellow = arsenic; the dotted yellow lines highlight the 3.32 Å separation distance between the square-pyramidal V atoms and the central As atom.

Spectroscopic Studies

Infrared spectrum. The infrared spectrum of the B-type Keggin anion, shown in Figure 4 is typical of that of a conventional Keggin anion, showing main absorptions in the expected spectral ranges. Nevertheless, careful comparative examination of experimental data supported by calculations makes it possible to extract reliable trends related to the B-

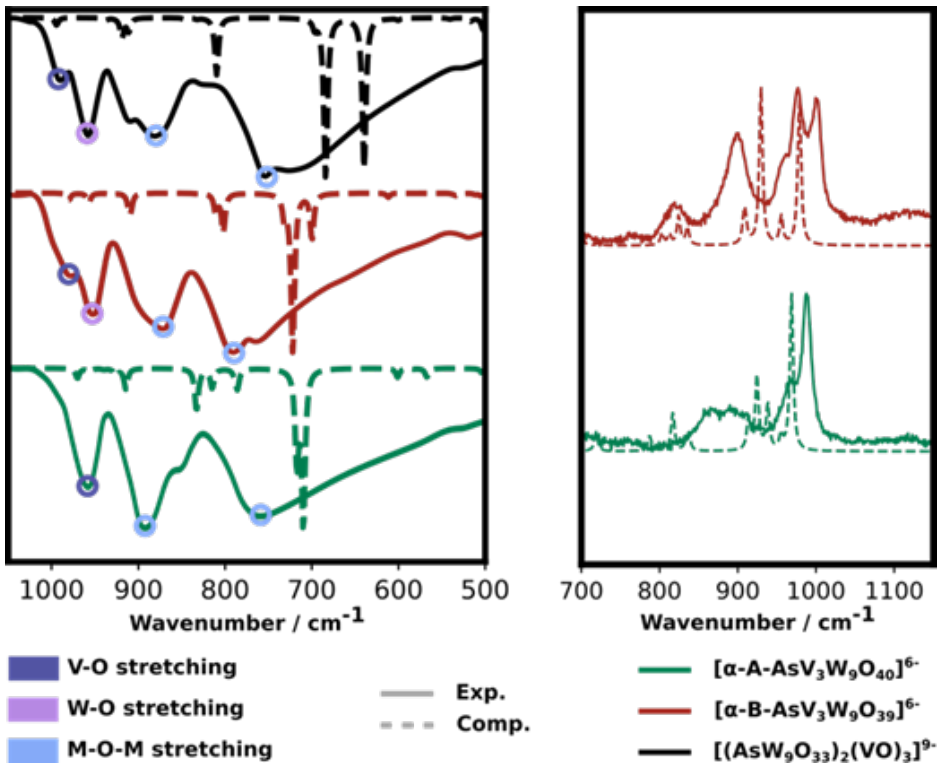

Figure 4. Left: experimental and calculated Infrared spectra of Keggin-type anions α-(1,2,3)-$[AsW_9V_3O_{40}]^{6-}$ (black) and α-(1,4,9)-$[AsW_9V_3O_{39}]^{6-}$ (red) compared to that of the sandwich-type compound $[(\alpha\text{-B-}AsW_9O_{33})_2(VO)_3]^{9-}$ (green). Superimposition of the three infrared spectra highlights significant differences in the region of the M=O stretching mode (ca. 1000 cm^{-1}), sensitive to the geometry of the V atom, octahedral in the A-type and square-pyramidal in the B-type and Sandwich type spectra. Right: experimental and calculated Raman spectra of the α-(1,4,9)-$[AsW_9V_3O_{39}]^{6-}$ (red line) and α-(1,2,3)-$[AsW_9V_3O_{40}]^{6-}$ (black line) anions acquired in aqueous solution.

type Keggin structure. The {M=O} vibrators give rise absorptions in the 950-1000 cm^{-1} corresponding to either symmetric or antisymmetric stretching modes.[39,40] The infrared spectrum of α-(1,4,9)-$[AsW_9V_3O_{39}]^{6-}$ reveals a strong absorption band at 952 cm^{-1} and a higher energy one at 977 cm^{-1} of medium intensity. Such a situation appears more pronounced with the sandwich compound which exhibits a strong band at 959 cm^{-1} and a medium one at 993 cm^{-1}. Nonetheless, in the conventional Keggin-type ion α-(1,2,3)-$[AsW_9V_3O_{40}]^{6-}$, only a single quasi-symmetric absorption is observed at 958 cm^{-1}, probably

due to the six-coordinated environment of the V atoms that reduces the wavenumber of the ν(V=O) stretching mode by the trans influence of the μ_3-Oa atom leading to closer ν(V=O) and ν(W=O) absorptions. Furthermore, computational studies are rather consistent with these observations showing that the ν(V=O) modes are quite sensitive to the environment of the V atom, increasing from 970 cm^{-1} for octahedral to 994 cm^{-1} for square-pyramidal geometry (see Figure 4A and ESI, Section S6, Table S3). Meanwhile, the remaining part of the infrared spectrum agrees that of Keggin-type ion showing absorptions attributed to the stretching of the bridging modes M-O-M at 872 cm^{-1} for the corner-shared junctions and at 747 and 794 cm^{-1} for the edge shared junctions. Furthermore, absorption related to the ν_{as}(As-O_a) mode is observed as a shoulder at 900 cm^{-1}. The calculated frequencies for the As-O vibration slightly differ from the experimental values. For the sandwich type, this vibration is located at 697 cm^{-1}. For the two different Keggin molecules the values are also different. The B-type Keggin absorbs at 731 cm^{-1} for the AsO_3 symmetrical stretching, while the conventional A-type Keggin has two absorptions at 833 and 828 cm^{-1} for antisymmetrical and symmetrical stretching respectively. In general, the computational IR spectrum is shifted to lower wavenumbers keeping the relative positions of the peaks.

Raman Spectrum. The Raman spectrum of the α-(1,4,9)-B-$[AsW_9V_3O_{39}]^{6-}$ anion in aqueous solution (see Figure 4) supports nicely the analysis given for the infrared data. This Raman spectrum reveals two intense bands that should correspond to two symmetrical M=O_d breathing modes, attributed respectively to {V=O} vibrations at 1002

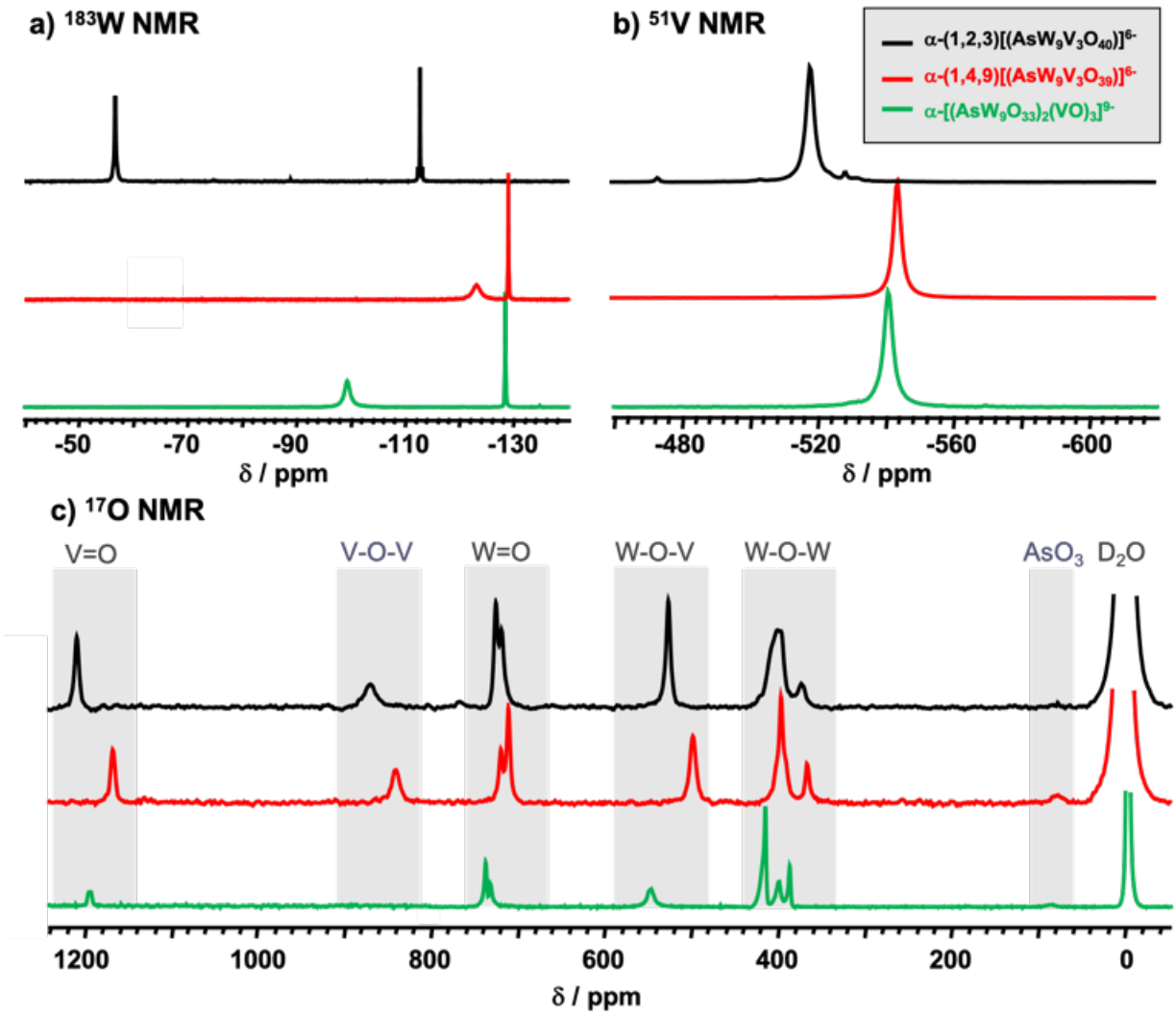

Figure 5. Multinuclear a) ^{183}W, b) ^{51}V, and c) natural abundance ^{17}O NMR spectra of the α-(1,4,9)-B-$[AsW_9V_3O_{39}]^{6-}$ anion in aqueous solution at room temperature (in red) compared with those of the α-(1,2,3)-A-$[AsW_9V_3O_{40}]^{6-}$ and α-B-$[AsW_9O_{33})_2(VO)_3]^{9-}$ anions in green and black, respectively.

cm^{-1} and {W=O_d} vibrations at 977 cm^{-1}. Conversely, the Raman spectrum of the α-(1,2,3)-$[AsW_9V_3O_{40}]^{6-}$ anion contains only one intense band at 967 cm^{-1}, consistent with the overlapped {V=O} and {W=O} vibrations within the breathing M=O_d mode. In addition, the distribution of V centres in the Keggin structure also modifies the 900-800 cm^{-1} region, which contains mainly antisymmetrical M-O-M vibrations, intense in the infrared and generally weak in the Raman mode.[40] Here, the presence of the three vanadium centres on

the {1,4,9} sites gives rise to two distinct bands observed at 902 and 867 cm^{-1}, while the {1,2,3} derivative produces the usual weak, broad and overlapped signal in the 900-800 cm^{-1} range observed with the conventional Keggin-type anion. Again, the absence of V-O_a interactions should significantly strengthen the V-O_c-V junctions with respect to the V-O-W and W-O-W junctions. This could explain the presence of these two absorptions attributed to both types of junctions. The calculated Raman spectrum also reveals the presence of two intense signals in the mentioned region. The signal for the A-type Keggin around 930 cm^{-1} represents several contributions from different absorptions, whereas they are differentiated in the experimental spectrum.

NMR (liquid state in D_2O solution). ^{51}V, ^{183}W and ^{17}O NMR spectra of the α-(1,4,9)-B-$[AsW_9V_3O_{39}]^{6-}$ anion and those of the two other POMs are shown in Figure 5. Analysis of these spectra removes any ambiguity as to the purity of the three compounds. The ^{51}V NMR spectra contain a single resonance for each case, consistent with the expected symmetry that makes the three vanadium nuclei equivalent. Nonetheless, the ^{51}V NMR chemical shift is quite sensitive to the environment of the V atom and could be influenced by its coordination number (CN) showing a systematic deshielding of the V nuclei as its coordination number increases from CN = 4 to 6.[41] Such a trend is nicely satisfied with a close chemical shift for both the α-(1,4,9)-B-$[AsW_9V_3O_{39}]^{6-}$ and α-B-$[(AsW_9O_{33})_2(VO)_3]^{9-}$ species observed at ca. δ = -544 and -541 ppm, respectively, where the V atoms adopt a square pyramidal geometry (CN = 5). Consistently, the V nuclei in the α-(1,2,3)-$[AsW_9V_3O_{40}]^{6-}$ undergoes a significant deshielding (δ = -518 ppm), in agreement with their octahedral geometry (CN = 6). The computational ^{51}V-NMR spectra show a single signal for each of the compounds studied, corresponding to the three vanadium atoms being

equivalent by the symmetry of the molecule. The calculated chemical shift is referred to the $VOCl_3$ reference using water as solvent. There is some discrepancy between the absolute values of experimental and calculated shifts, but the general trend is consistently maintained. In addition, the ^{51}V NMR linewidth also provides relevant information since the relaxation rate of the quadrupolar nuclei depends on the electric field gradient generated by the surrounding atoms, and therefore reflects the symmetry of the coordination sphere of the V nuclei. In this present case, the ^{51}V NMR linewidths of the three compounds lies in a narrow range ($\Delta\nu_{1/2}$ = 240-300 Hz) that makes difficult any qualitative explanation arising from the geometrical environment of the V nuclei. Nevertheless, ^{51}V NMR in the liquid state could be useful for highlighting protonation processes involving the most basic oxygen atoms of the metal-oxo framework, generally corresponding to those belonging to the first coordination shell of the vanadium centres.[35,42] Variation of the ^{51}V NMR chemical shift *vs* pH is given in the ESI, Section S7.1. For the α-(1,4,9)-$[AsW_9V_3O_{39}]^{6-}$ anion, the plot is consistent with a protonation process featured by a *p*Ka value close to 1, while the other vanadium Keggin-type anion, the α-(1,2,3)-$[AsW_9V_3O_{40}]^{6-}$ exhibits a significantly higher value (*p*Ka = 2.25). Such a difference should arise from the specific environment of the three vanadium centres where the μ_3-oxo group is missing within the $\{V_3\}$ cap, causing the decrease of the electronic density on the remaining oxo groups.

Furthermore, the ^{183}W NMR spectra of the three compounds contain two resonances with 1:2 intensity ratio for each case, consistent with C_{3v} local symmetry of the $\{AsW_9\}$ subunits. However, the ^{183}W NMR spectra of both vanadium-containing anions built from the B-type $\{AsW_9O_{33}\}$ subunits give similar pattern with a substantial line broadening ($\Delta\nu_{1/2}$ = 30-35Hz) for the resonance attributed to the six equivalent tungsten atoms due to edge-shared coupling with the ^{51}V nuclei. Besides, the remaining resonances attributed to

the three remaining equivalent W nuclei exhibit usual linewidth of 1-2 Hz and gives very close chemical shift ($\delta < 1$ ppm). Such an observation results from their location far enough from vanadium nuclei. These signals also exhibit satellite doublet due to $^{2}J_{W\text{-}W}$ coupling of 6 Hz characteristic of the W-O-W edge shared junctions present in the α-B-{AsW_9O_{33}} subunit (see ESI, Section S1), which is significantly different from the $^{2}J_{W\text{-}W}$ coupling value of 17 Hz observed in the α-(1,2,3)-$[AsW_9V_3O_{40}]^{6-}$ anion built with W-O-W junctions through shared corners.[43] The ^{17}O NMR spectra of the three species are given in Figure 5c showing the attributions to the individual oxygen sites. These attributions were established on the basis of experimental[44] and theoretical[45] literature data, and were supported by the calculations from this study presented in the ESI, Section S7.2, Table S5. As previously observed in the ^{51}V and ^{183}W NMR study, the ^{17}O NMR spectra of the compounds (1,4,9)-$[AsW_9V_3O_{39}]^{6-}$ and $[(AsW_9O_{33})_2(VO)_3]^{9-}$ show similar signatures, but with one notable exception, namely that the spectrum of the polyanion (1,4,9)-$[AsW_9V_3O_{39}]^{6-}$ additionally exhibits a resonance at around 850 ppm. The latter is reasonably attributed to the ^{17}O nuclei of the V-O_c-V junctions, which do not exist in the compound $[(AsW_9O_{33})_2(VO)_3]^{9-}$. The ^{17}O NMR spectrum of the Keggin (1,2,3)-$[AsW_9V_3O_{40}]^{6-}$ anion shows a resonance associated with the oxygen atoms bridging the vanadium atoms in a region close to that observed for the Keggin B-type ion. Overall, the

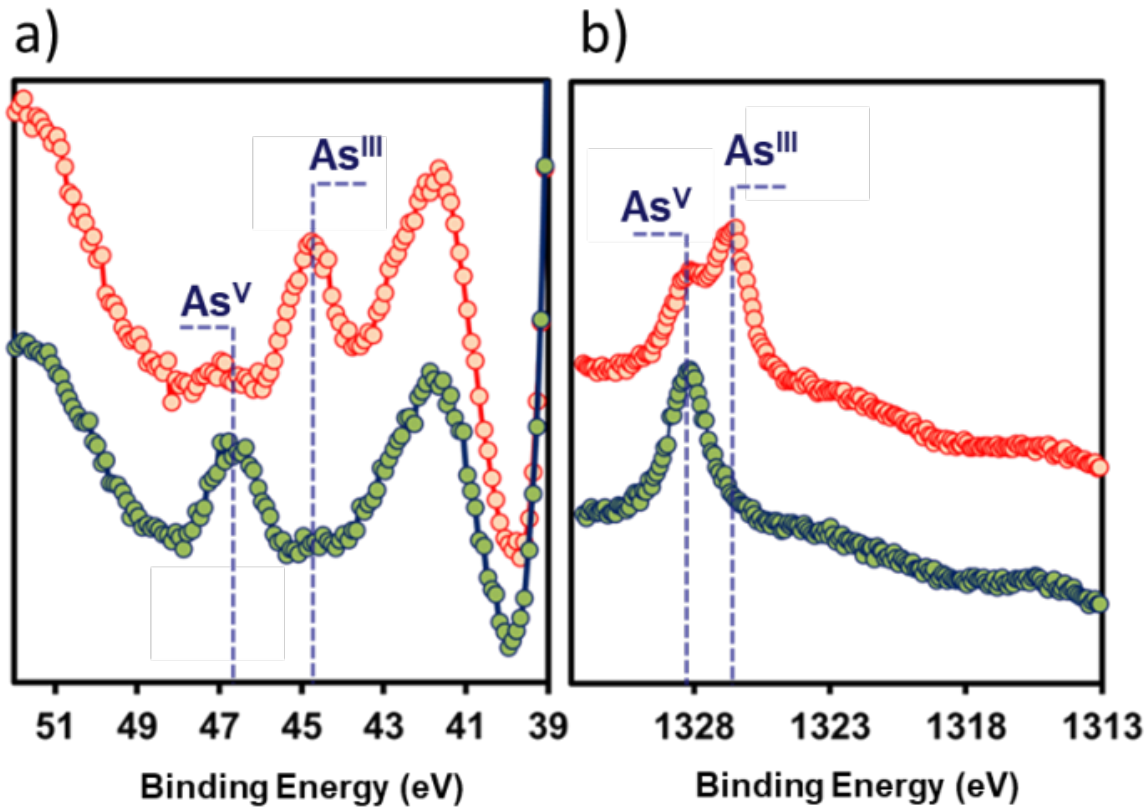

Figure 6. X-ray photoelectron spectra of the α-(1,4,9)-$[AsW_9V_3O_{39}]^{6-}$ (red trace) and α-(1,2,3)-$[AsW_9V_3O_{40}]^{6-}$ (green trace) anions as potassium salts. a) Low energy region highlighting distinctly the As $3d_{5/2}$ signals characteristic of As^V (46.7 eV) or As^{III} (44.7 eV) within the α-(1,2,3)-$[AsW_9V_3O_{40}]^{6-}$ and α-(1,4,9)-$[AsW_9V_3O_{39}]^{6-}$ anions, respectively; b) High energy region (As $3p_{3/2}$) showing substantial presence of As^V in the top monolayer of the K_6α-(1,4,9)-$[AsW_9V_3O_{39}]$ phase. At the same time, the α-(1,2,3)-$[AsW_9V_3O_{40}]^{6-}$ species exhibits unambiguously a single peak attributed to the presence As^V.

^{17}O NMR spectra of the Keggin ions are very similar. From the computational point of view, the ^{17}O NMR spectra can help to assign the experimental signals. The agreement between the computed and experimental spectrums is very high and reproduces the relative position of the signals with very few differences in ppm. It is noteworthy that the signal corresponding to the V=O oxygen is sensitive to the coordination sphere of the vanadium atom, showing a similar chemical shift of the oxygen bound to the square pyramidal V, and different to the octahedral case in the A-type. Moreover, the V-O-V oxygen signals are also affected by the coordination of the V atom, with a difference of 90 ppm between the

octahedral and square pyramidal cases. The same behaviour is observed in the O signals corresponding to the V-O-W sites. A difference of 80 ppm is observed when comparing the Keggin B-type with the A-type equivalent, and 100 ppm with the POM sandwich.

XPS Experiments. X-ray photoelectron spectroscopy (XPS) has been carried out to get definitive evidence about the oxidation state of the arsenic ion within the Keggin-type species. For this purpose, both As $3d_{5/2}$ and As $2p_{3/2}$ spectral regions were recorded. Photoelectron inelastic mean free path (IMFP) was estimated for the two As considered peaks, according to TPP2M formula.[39,40] With an IMFP of 0.6 nm, the As $2p_{3/2}$ core level probes mainly the upper surface of the material while As 3*d* peak with an IMFP of 2.7 nm is then more representative of the "bulk". Figure 6a shows the XPS signature of the two Keggin-type compounds in the As 3*d* spectral region. For α-(1,2,3)-$[AsW_9V_3O_{40}]^{6-}$ species, the spectrum evidences a single low spin-orbit splitting doublet centred at 46.7 eV, which is characteristic of the As^V oxidation state.[41] Such a situation contrasts significantly with the α-(1,4,9)-$[AsW_9V_3O_{39}]^{6-}$ species. Even if a weak As^V signal is visible at 46.7 eV, the As $3d_{5/2}$ spectrum is dominated by a similar doublet but shifted to lower binding energy (44.7 eV). This energy position is consistent with As atoms at +III oxidation state.[41] The XPS analyses conducted in the high binding energy domain (see Figure 6b) confirm this trend. While the As $2p_{3/2}$ signal of the As(V) containing Keggin-type anion showed, as expected, only a single peak at 1328.1 eV, according to the presence of As(V), those of the As^{III}-containing anion reveal two contributions at 1328.1 and 1326.5 eV, respectively indicative of the concomitant presence of As^V and As^{III} species.[42] Since this core level is mostly representative of the top-surface composition, the

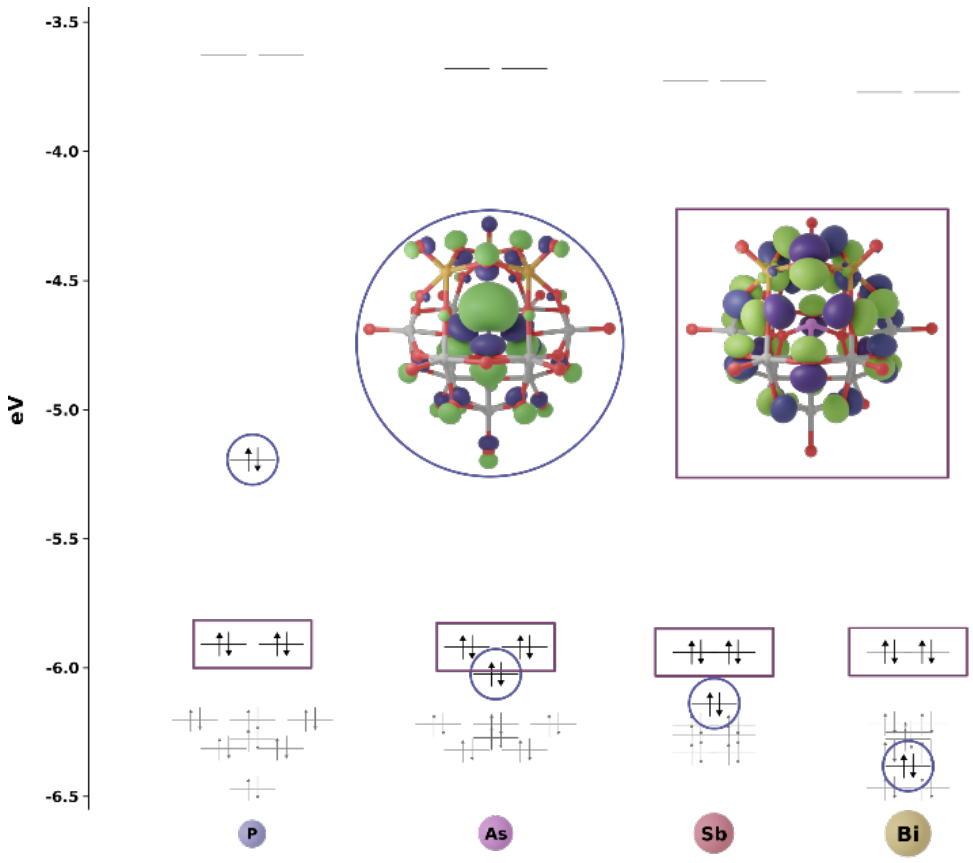

Figure 7. Frontier molecular orbitals energy levels for the α-(1,4,9)-[$XW_9V_3O_{39}]^{6-}$ (X = P, As, Sb, Bi) anions. Molecular orbital representations for the heteroatom lone-pair orbital (circled) and the HOMO for the As derivative (squared).

greater relative proportion of As^{V} compared to As^{III} highlights the spatial distribution of As atoms. The bulk of this Keggin-type compound is composed of As^{III} while As^{V} atoms are located at the surface of the crystals. Since no particular precaution was taken prior surface analysis, a partial surface oxidation or pollution cannot be excluded in the present case.

Electronic Structure. In addition to the geometric and electronic structure of the α-(1,4,9)-$[AsW_9V_3O_{39}]^{6-}$ anion, we also considered the hypothetical P, Sb and Bi analogues. Their frontier molecular orbitals energy levels are pictured in Figure 7. For the P derivative, the HOMO is the heteroatom lone-pair orbital (circled) clearly localized in the heteroatom as depicted in Figure 7. The energy of this lone-pair orbital decreases along the series while the energy of the oxo-band typical in polyoxometalates is hardly affected. Consequently, the HOMO for As, Sb and Bi is not located in the lone-pair orbital anymore but in the orbitals belonging to the oxygen atoms. In all cases, the LUMO orbital corresponds to the fully oxidized W atoms, i.e., the empty d-band, typical of metal-oxo clusters. Along the series, we observed a slight stabilization of the LUMO level. In all, the smallest HOMO-LUMO gap corresponds to the P species, and the largest to the As system. According to our calculations, although the gap decreases when going

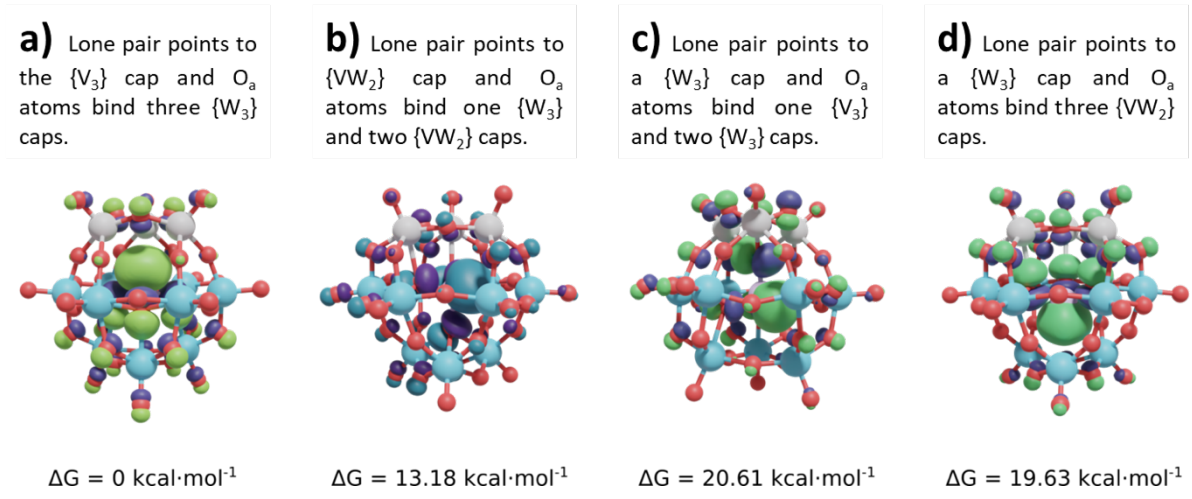

Figure 8. Optimized geometries of the four isomers corresponding to the different $\{AsO_3\}$ orientation inside the $\{W_9V_3O_{36}\}$ metal-oxo shell. All Gibbs free energies (kcal·mol^{-1}) are compared to the isomer a) where the lone pair orbital of the As^{III} atom points toward the $\{V_3\}$ triad. Color code: red for the Oxygen, gray for the Vanadium, light blue for the Molybdenum and purple for the As.

from As to Bi, we predict similar stability for the Sb and Bi hypothetical analogues as for As compound, and much smaller for P derivative. These differences should be observed in the electronic properties.

In addition, several positional isomers could be generated virtually by the successive change of the $\{AsO_3\}$ orientation in the $\{W_9V_3O_{36}\}$ oxometallic cage. Such a theoretical study is of interest for assessing the energy cost when the square pyramidal geometry changes from a vanadium to a tungsten center. Then, four isomers were identified in which the electronic lone-pair of the central As(III) atoms was successively directed toward the different types of metallic triads, i.e. $\{V_3\}$, $\{VW_2\}$ or $\{W_3\}$ caps as shown in Figure 8. The geometry was optimized for all four isomers and the Gibbs free energies were calculated and referenced to the first isomer. Results of these calculations showed clearly that the most stable arrangement is obtained when the lone-pair is directed toward the three vanadium cap. Changing the $\{AsO_3\}$ orientation leads to a second isomer with the lone pair pointing toward a $\{VW_2\}$ triad. Then, the resulting compound contains two W and one V centers which adopt a square pyramidal geometry. Such a change results in a significant decrease of the intrinsic stability, featured by an energy difference close to ~13 kcal·mol^{-1} (see Figure 8). The other two remaining isomers both exhibit in their structure three square pyramidal W centers in a trimetallic cap. The consequences of these configurations clearly correspond to a large energy increase of ~20 kcal·mol^{-1} for both. These results therefore suggest that the square pyramidal geometry for W^{VI} atoms is energetically very demanding compared to V^{V} atoms, which is in perfect agreement with what was found experimentally.

Electrochemical Behavior and Electronic Spectra. The cyclic voltammograms of the α-(1,4,9)-$[AsW_9V_3O_{39}]^{6-}$ anion have been measured in various buffered aqueous solutions

with pH values varying from about 1 to 9. Its CV reveals the typical pattern expected for a three vanadium-containing anion which should be understood as three

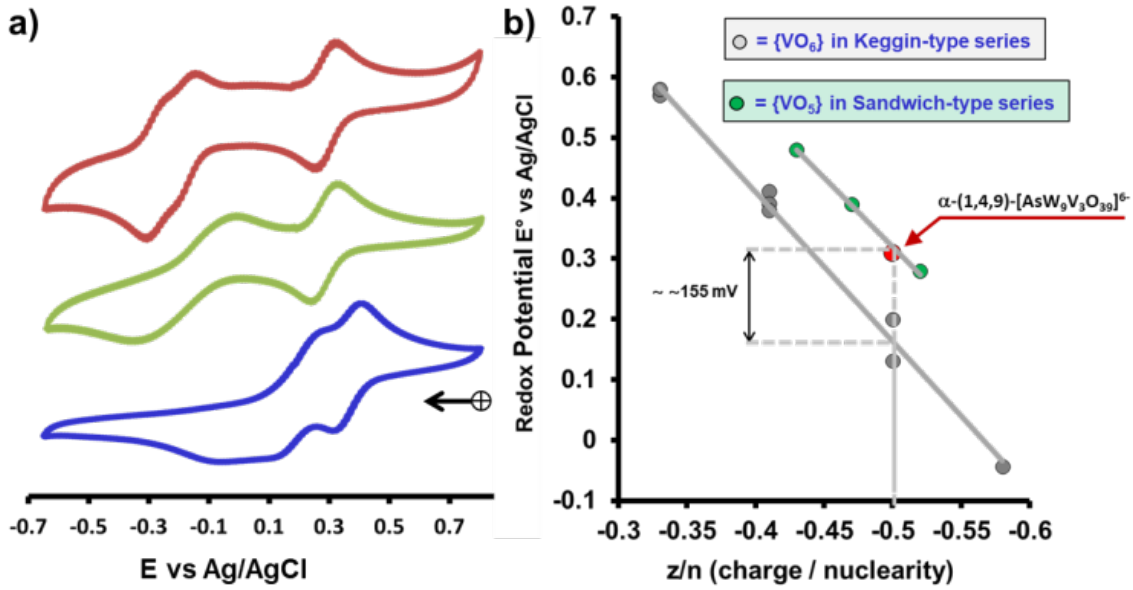

Figure 9. a) Cyclic voltammograms of the studied vanadium-containing anion α-(1,4,9)-$[AsW_9V_3O_{39}]^{6-}$ collected in aqueous solution buffered with acetate/acetic acid, *p*H = 4.75 (blue trace), TRIS/HTRIS, *p*H = 7.75 (green trace) and NH_3/NH_4Cl, *p*H = 9.10 (red trace). b) *p*H-independent reduction potentials for Keggin anions as a function of z/n parameter with z corresponds to the anion charge and n the metal centre nuclearity of the anion. Depending on the geometry of the vanadium centre within the Keggin derivatives, two distinct linear correlations are highlighted revealing that the oxidizing character of the square-pyramidal $\{VO_5\}$ groups is about 155 mV higher than that of the $\{VO_6\}$ arrangements.

successive one-electron transfers (see Figure 9). While the first electron transfer appears quasi-reversible and nearly pH non-dependant ($E° = 0.300$ V vs. Ag/AgCl, $\Delta P_{a-c} = 60$ mV), the two following redox events corresponding to the formation of the two and three-electron reduced species appear nearly irreversible featured by two cathodic peaks located at +0.14 and -0.069 V *vs.* Ag/AgCl and by a single anodic wave at +0.29 V *vs*. Ag/AgCl. Although it has been established that the redox potentials characterizing electron transfers in POMs

depend primarily on the electron charge density, the geometry of the vanadium centre also impacts the electronic structure and consequently alters the electrochemical properties. In turn, a nice opportunity is given here to investigate the influence of the square pyramidal $\{VO_5\}$ versus octahedral $\{VO_6\}$ geometry upon the electron transfer processes involving the V^V/V^{IV} couple. Therefore, we compared a wide selection of V^V/V^{IV} redox potential corresponding to the first electron transfer under no protonation condition, involving either octahedral or square-pyramidal geometry. Nevertheless, these redox potentials have been plotted against the parameter z/n (see Figure 8b, where z correspond to the ionic charge fraction and n the metal centre nuclearity of the POM species which corresponds to 12 for the Keggin type-anion or 21 for the sandwich-type species. In fact, this parameter is useful for simply estimating the charge density of the anion, which is necessary to discriminate any contribution from geometry or charge density. Interestingly, graphical representation of E° as function of z/n shows two distinct and nearly parallel linear correlations which correspond to $\{VO_6\}$-containing Keggin-type series and to the $\{VO_5\}$-sandwich type series, respectively. All the details, information and references concerning the electrochemical data used in Figure 9b are given in ESI, Section 8. In addition, it should be noted that our anion α-(1,4,9)-$[AsW_9V_3O_{39}]^{6-}$ belongs fairly to the $\{VO_5\}$ correlation, in line with the assumed square pyramidal geometry of its three vanadium centres. Besides, such a graphical representation reveals that $\{VO_5\}$ centres are intrinsically more oxidant than $\{VO_6\}$ arrangements. This finding is probably a consequence of the electron density in the vicinity of the V centre, which should be higher in $\{VO_6\}$ than in $\{VO_5\}$. Finally, the linear variation in redox potential for the two series of POMs containing vanadium is consistent with the results previously established by Pope et al.[43] Furthermore, the CV of the α-(1,4,9)-$[AsW_9V_3O_{39}]^{6-}$ reveals additional redox events according to the reduction of

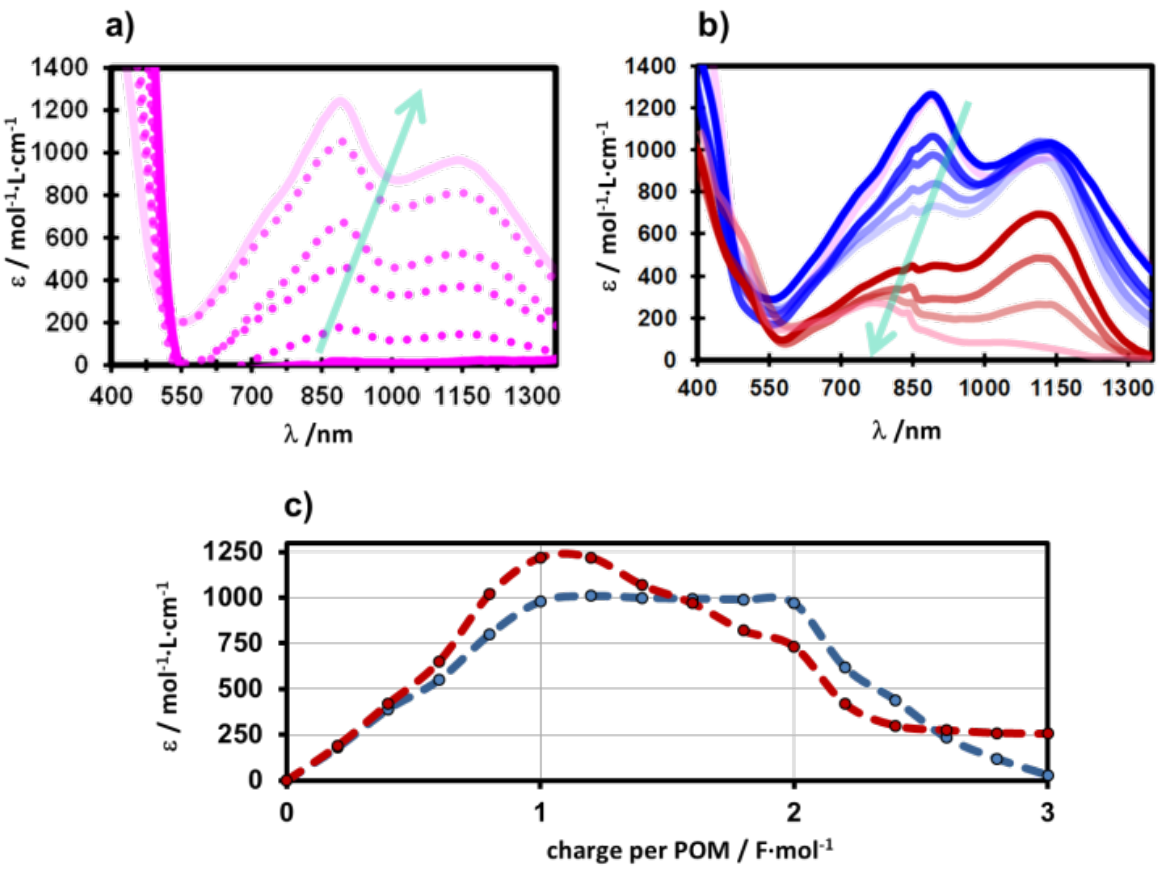

Figure 10. Spectroscopic features in the visible-NIR range of the B-type anion α-(1,4,9)-$[AsW_9V_3O_{39}]^{6-}$ measured in aqueous solution at *p*H = 4.75, during reductive electrolysis experiment: a) Growth in the IVCTs characterized by λ_{max} = 1150 nm (8 700 cm-1) and 890 nm (11 200 cm^{-1}) for n varying from 0 to 1; b) decrease in IVCTs when the reduction process progresses from 1 up to 3. c) Variation of the molar absorption coefficient ε of IVCT maxima at 1150 nm (red curve) and at 890 nm (blue curve) evidencing three distinct domains separated by the four redox states n = 0, 1, 2 and 3.

the two-remaining vanadium (V) into vanadium (IV) (see Figure 8a). These two one-electron transfers exhibit a weak reversibility at *p*H lower than 8 while at *p*H = 9.10, they appear fairly reversible (ΔP_{a-c} ~ 60 mV). This evidences that one of the causes of irreversibility probably arises from protonation processes concomitant to the electron

transfer which are known to distort the coordination sphere of the vanadium center by lengthening the V-O bond and closing angle of the V-O-V bridge.[25,44]

Spectro-electrochemistry experiments were also carried out, giving information about the resulting V^{V}/V^{IV} mixed-valence system. Reduction of the anion was carried out in acetate buffer (*p*H = 4.7) through electrolysis at controlled potential carbon electrode (-0.7 V vs Ag-AgCl), allowing the successive reduction of the three vanadium (V) centers into vanadium (IV). The resulting UV-vis spectra in the region above 600 nm are characteristic of the mixed-valence V^{V}/V^{IV} system (see Figure 10a). As the charge consumed per POM (noted n) increases from 0 to 1, two distinct peaks located at 11 200 cm^{-1} (890 nm) and 8700 cm^{-1} (1150 nm) grow continuously while the electrolysis solution undergoes a color change from orange to green. Attribution of both absorptions is consistent with intervalence charge transfer (IVCTs) $V^{IV} \rightarrow V^{V}$ while those corresponding to $V^{IV} \rightarrow W^{VI}$ are located in higher energy range (not shown).[45] Then, these two absorptions reach their maximum intensity for n = 1. The intensity of the lower energy absorption at 8 700 cm^{-1} remains quite constant (ε = 1 000 $mol^{-1} \cdot L \cdot cm^{-1}$) until n = 2, while that of the other (11 200 cm^{-1}) decreases significantly from 1 220 to 730 $mol^{-1} \cdot L \cdot cm^{-1}$. At last, above n = 2, both absorptions undergo an abrupt decrease of their intensity in agreement with the expected cancel of the V^{IV}/V^{V} IVCTs. As the lower energy absorption gives an intensity close to zero for n = 3, the other undergoes a gradual shifted in energy from 11 200 cm^{-1} (890 nm) to 12 800 cm^{-1} (780 nm) and reaches a minimum intensity value corresponding to molar absorption coefficient ε = 260 $mol^{-1} \cdot L \cdot cm^{-1}$ for three V^{IV} ions. It should be noted that this residual absorption is fully consistent in energy (12 800 cm^{-1}) and intensity (ε = 85 $mol^{-1} \cdot L \cdot cm^{-1}$ per V^{IV} ion) with contribution of d-d transitions predicted for the $\{V{=}O\}^{2+}$ vanadyl species[46] and previously reported in the literature.[34] Besides, variation of the molar extinction coefficient as function

of transferred charge per POM, shown in Figure 10b is fully representative of the three redox states corresponding to 1-, 2- and 3-electron reduced species.

CONCLUSIONS

In this report, we have summarized experimental and theoretical efforts to provide complementary insights into structural, spectroscopic and electrochemical properties of a new Keggin B-type anion based on a $\{AsW_9O_{33}\}$ subunit capped by a vanadium triad $\{V_3O_6\}$. Experimental evidence supported by theoretical calculations has unequivocally revealed the nature, location and geometry of the three vanadium atoms, embedded within the Keggin-type framework. These results showed clearly that changing the geometry of the vanadium atom from octahedral to square pyramidal leads to a significant increase of its oxidant behaviour by about 155 mV. This should have important impact for the design of vanadium-based electrodes or composition of vanadium-based electrolytes involved within redox flow batteries. Moreover, this O-deficient Keggin archetype for mixed metals should not be restricted to this example, since polyoxometalate chemistry allows structures containing the typical square pyramidal environment $\{O=MO_4\}$. For instance, niobium (V)-based POMs should be good candidates[47,48] but the series could be even extended to molybdenum and tungsten derivatives.[28] In this context, our theoretical and experimental research currently being carried out aims to understand the general behavior of these O-deficient Keggin species on the basis of their electronic and physicochemical properties.

EXPERIMENTAL SECTION

Materials and Methods.

Fourier Transform Infrared (FT-IR); Spectra were recorded on a 6700 FT-IR Nicolet spectrophotometer, using diamond ATR technique. The spectra were recorded on non-diluted compounds and ATR correction was applied.

Raman spectroscopy. An air-cooled diode laser (LaserOne, 532 nm, 100 mW) was used as an excitation source. Raman experiments were conducted on a custom delivered Raman probe (SuperHead fiber optic probe, Horiba Scientific), consisting of edge and interference filters for the 532 nm laser, focusing and collecting lens with 55 mm focal length and two optical fiber connections for the laser and the spectrometer, placed in front of a quartz cuvette containing Keggin-type species dispersed in water. The Raman scattered photons were then analyzed via a spectrometer (iHR-320, 320 mm focal length, Horiba Scientific) coupled with a CCD detector (Syncerity, Horiba Scientific) cooled by Peltier effect. For all measurements a Raman laser power of 100 mW, spectrometer grating of 1800 gr/mm, slit width of 98 μm and exposure time of 5 s were used.

Elemental analyses. Quantitative analyses of metal contents were carried out by ICP analysis performed in CREALINS laboratory in Vernaison, France.

Energy-dispersive X-ray spectroscopy. EDS measurements were performed using a SEM-FEG (Scanning Electron Microscope enhanced by a Field Emission Gun) equipment (JSM 7001-F, Jeol). The measures were acquired with a SDD XMax 50 mm^2 detector and the Aztec (Oxford) system working at 15 kV and 10 mm working distance. The quantification is realized with the standard library provided by the constructor using Lα lines.

Thermal gravimetric analysis (TGA). To determine water content, a Mettler Toledo TGA/DSC 1, STAR^e System apparatus was used under oxygen flow (50 mL min^{-1}) at a heating rate of 5 °C min^{-1} up to 700 °C.

Single-crystal X-ray diffraction. Intensity data collections were carried out at T = 200(2) K with a Bruker D8 VENTURE diffractometer equipped with a PHOTON 100 CMOS bidimensional detector using a high brilliance IμS microfocus X-ray Mo Kα monochromatized radiation (λ = 0.71073 Å). Crystals were glued in paratone oil to prevent any loss of crystallization water. Data reduction was accomplished using SAINT V7.53a. The substantial redundancy in data allowed a semi-empirical absorption correction (SADABS V2.10) to be applied, on the basis of multiple measurements of equivalent reflections. Using Olex2,[49] the structure was solved with the ShelXT[50] structure solution program using Intrinsic Phasing and refined with the ShelXL refinement package using Least Squares minimization. Heavier atoms (W) for each structure were initially located by direct methods. The remaining nonhydrogen atoms were located from Fourier differences and were refined with anisotropic thermal parameters. Thereby the contribution of solvent-electron density was removed using the SQUEEZE routine in PLATON, producing a set of solvent-free diffraction intensities. Crystallographic data for single-crystal X-ray diffraction studies are summarized and details about the refinements of the crystal structure are included in the section 4. These data can be obtained free of charge from The Cambridge Crystallographic Data Centre via https://www.ccdc.cam.ac.uk/structures-beta/. Deposit number: 2382113.

Electrochemistry. Deionized water was used throughout the process. It was obtained by passing water through a RiOs 8 unit followed by a Millipore-Q Academic purification set. All reagents were of high-purity grade and were used as purchased without further purification. Cyclic voltammetric (CV) experiments were carried out with an Methrohm Autolab PGSTAT12 potentiostat/galvanostat associated with a GPES electrochemical analysis system (EcoChemie). Measurements were performed at room temperature in a

conventional single compartment cell. A glassy carbon (GC) electrode with a diameter of 3 mm was used as the working electrode. The auxiliary electrode was a Pt plate placed within a fritted-glass isolation chamber and potentials are quoted against a saturated calomel electrode (SCE). The solutions were deaerated thoroughly for at least 30 minutes with pure argon and kept under a positive pressure of this gas during the experiments.

Nuclear Magnetic Resonance (liquid NMR). All solution NMR spectra were measured in D_2O at 26 °C. ^{51}V and ^{17}O NMR spectra were obtained on a Bruker Avance 400 spectrometer at Larmor frequencies of 105.1 and 54.3 MHz, respectively, using 5 mm standard NMR tubes. The spectra were recorded with one pulse sequence at 90° flip angle (pulse duration 11 or 20 μs), using 0.1 s recycle delay, an acquisition time of 80 or 40 ms, and ca 1000 or 4000000 scan numbers, for ^{51}V and ^{17}O NMR, respectively. The ^{183}W NMR spectra were obtained on a Bruker AVANCE 500 MHz spectrometer using a 10 mm NMR tube, accumulating 32000 scans of 37 μs-pulse (90° flip angle) with an acquisition time of 2 s, and a relaxation delay of 1 s. Chemical shifts are reported relative to external standards (δ = 0 ppm), 90% $VOCl_3$ in C_6D_6 for ^{51}V, H_2O for ^{17}O, and 1 M Na_2WO_4 aqueous solution for ^{183}W.

X-ray photoelectron spectroscopy. Few milligrams of material were deposited on conductive tape for analysis purpose. Regular XPS analyses were conducted on a Thermofisher Scientific Nexsa equipped with a monochromated Al-Kα anode (1486.6 eV) and a dual flood gun (low energy electron and ion). High energy resolution spectral windows of interest were recorded with a 400 μm spot size. The photoelectron detection was performed perpendicularly to the surface using a constant analyzer energy (CAE) mode (20 eV pass energy) and a 0.1 eV energy step.

UV-vis spectroscopy. UV−vis spectra of solutions were recorded at room temperature on a PerkinElmer Lambda 750 using calibrated 0.1 cm quartz cell.

Computational details. The molecular geometries of all polyoxometalates were fully optimized employing the ADF[51] software package (SCM ADF version 2021.101), using the BP86[52,53] functional, with the relativistic corrections related to the scalar-relativistic zero-order regular approximation (ZORA),[54,55] using a TZP basis set level. Solvation effects were introduced by means of the continuous solvent model COSMO with Klamt[56] radii for water. Stationary points were characterized with analytic frequency calculations. All Gibbs free energies were computed at 298.15 K and 1 atm, using the ideal gas-rigid rotor-harmonic oscillator (IGRRHO) model. NMR chemical shifts[57-59] were computed using the ADF sofware package (SCM ADF version 2021.101), employing the OPBE[60] functional and a TZP basis set. Solvation effects were considered using the COSMO model with the Klamt radii. A dataset collection with all DFT calculations is available in the ioChem-BD[61] repository via the following link http://dx.doi.org/10.19061/iochem-bd-1-338.

Synthesis of the compounds

The B- and A-type trivacant precursors, *i.e.* $Na_9[\alpha\text{-B-}As^{III}W_9O_{33}]\bullet 19\ H_2O$ and $Na_9[\alpha\text{-A-}As^{V}W_9O_{34}]\bullet 18\ H_2O$ have been synthesized according to reported procedures.[62-64]

$K_6[\alpha\text{-}(1,4,9)\text{-}As^{III}W_9V^{V}_3O_{39}].14H_2O$. Sodium metavanadate (0.74 g; 6.07 mmol) is dissolved in 15mL of water. The solution is heated at 50 °C and aqueous acetic acid solution (4 M; 6 mL) is added until pH drops to 3.4. The solution turned orange. Then $Na_9As^{III}W_9O_{33}\bullet 19\ H_2O$ (5 g; 1.90 mmol) was added progressively leading to pH increase up to 4.1. The solution is kept under heating and stirring during 1 h. The color turned slightly to red and the pH increased until 4.3. The solution was cooled at room temperature and KCl (3.5 g; 480 mmol) was added under slow stirring provoking the precipitation of an orange solid. The solution was cooled in ice and stirred slowly

during 1 h. The solid was then filtered, washed with EtOH and dried with Et_2O. The crude orange powder (3.1 g) was redissolved in 20 mL of water. After filtration, the clear resulting solution was allowed to stand for crystallization at room temperature. After four days, well-shaped orange crystals (2.4 g) corresponding to $K_6AsW_9V_3O_{39}$•14 H_2O were collected by filtration and washed with cold water. Yield: 42 % (based on W content). Anal. % Cald. (found): K, 7.8 (7.2) ; V, 5,1 (5.5) ; As, 2.5 (2.2) ; W, 55.3 (55.9); H_2O, 8.4 (8.3).

K_4H_2[α-(1,2,3)-$As^VW_9V^V_3O_{40}$].22H_2O. Sodium metavanadate (1,6 g ; 13,11 mmol) is dissolved in 50 mL of water at 50 °C. After complete dissolution, hydrochloric acid aqueous solution (2 M; 2.2 mL) is added slowly until pH drops to 1.5. Then, $Na_9[AsW_9O_{34}]$•18H_2O (11.4 g ; 4.37 mmol) is added into the solution under vigorous stirring. After complete dissolution, the color changes to give an intense red solution and pH is readjusted to 1.5 by the addition of an aqueous HCl solution (6 M). After 60 min, successive addition of potassium chloride solid (20 g; 270 mmol) and methanol lead to the formation of abundant orange-yellow solid (12-13 g after washing and drying by using ethanol and diethyl ether oxide). This solid is redissolved in 30 mL of distilled water at room temperature. The resulting solution is filtered by using a sintered glass frit to removed insoluble materials. The limpid red solution is cooled by an ice bath, allowing it to stand for crystallization. After 120 min, crystalline solid corresponding to K_4H_2[α-A(1,2,3)$As^VW_9V^V_3O_{40}$].22H_2O is collected by filtration. Yield: 4 g; 29% based on W. Anal. % calcd. (obs.) for $W_9V_3AsK_4H_{46}O_{62}$: K, 5.1 (5.4) ; V, 5.0 (5.3) ; As, 2.4 (2.2) ; W, 53.8 (53.4); H_2O, 12.9 (12.6).

ASSOCIATED CONTENT

Supporting Information

The Supporting Information is available free of charge at https://pubs.acs.org/doi/10.1021/acs.inorgchem.4c05330. Additional experimental details, materials, and methods, including computational details, IUPAC numbering, X-ray diffraction analysis and refinement, structural representations, vibrational spectroscopies (experimental and theoretical), multinuclear liquid NMR (*P*ka's determination and calculated NMR chemical shifts), electrochemical analysis.

Data availability

A dataset collection with all DFT calculations is available in the ioChem-BD repository[61] via the following link http://dx.doi.org/10.19061/iochem-bd-1-338.

AUTHORS INFORMATION

Corresponding authors

Mohamed Haouas - Institut Lavoisier de Versailles, UMR 8180 CNRS, UVSQ, Université Paris-Saclay, Versailles, France. E-mail : mohamed.haouas@uvsq.fr.

Carles Bo - Institute of Chemical Research of Catalonia (ICIQ). The Barcelona Institute of Science and Technology. Av. Països Catalans 16, 43007 Tarragona, Spain. E-mail: cbo@iciq.cat

Emmanuel Cadot - Institut Lavoisier de Versailles, UMR 8180 CNRS, UVSQ, Université Paris-Saclay, Versailles, France. E-mail : emmanuel.cadot@uvsq.fr.

Authors

Dr. Fa Ibrahima Bamba, Institut Lavoisier de Versailles, UMR 8180 CNRS, UVSQ, Université Paris-Saclay, Versailles, France.

Dr. Clément Falaise, Institut Lavoisier de Versailles, UMR 8180 CNRS, UVSQ, Université Paris-Saclay, Versailles, France.

Dr. Nathalie Leclerc, Institut Lavoisier de Versailles, UMR 8180 CNRS, UVSQ, Université Paris-Saclay, Versailles, France.

Pr. Dr. Gildas Gbassi, UFR Sciences Pharmaceutiques et Biologiques (UFR SPB), Université Félix Houphouet Boigny (UFHB), Abidjan, Côte d'Ivoire.

Dr. Patrick Atheba, UFR Sciences des Structures de la Matière et Technologie (UFR SSMT), Université Félix Houphouet Boigny (UFHB), Abidjan, Côte d'Ivoire.

Dr. Mathieu Fregnaux, Institut Lavoisier de Versailles, UMR 8180 CNRS, UVSQ, Université Paris-Saclay, Versailles, France.

Jordi Buils, Institute of Chemical Research of Catalonia (ICIQ). The Barcelona Institute of Science and Technology. Av. Països Catalans 16, 43007 Tarragona, Spain & Departament de Química Física I Inorgànica. Universitat Rovira I Virgili. c/Marcelí Domingo s/n, 43007 Tarragona, Spain.

Dr. Mireia Segado-Centellas, Departament de Química Física I Inorgànica. Universitat Rovira I Virgili. c/Marcelí Domingo s/n, 43007 Tarragona, Spain.

Authors contribution

Dr. Fa Ibrahima Bamba, experimental tasks such as synthesis of the compounds, electrochemistry, NMR, TGA, IR-FT, ICP elemental analysis.

Dr. Clément Falaise, experimental studies and related analyses, including single crystals X-ray structure analysis, electrochemistry, UV-vis, Raman and infrared spectroscopies. Contribution to the writing of the manuscript.

Dr. Nathalie Leclerc, supervision of the experimental tasks including chemical synthesis, electrochemistry, thermal and elemental analyses.

Dr Mohamed Haouas, supervision of the liquid NMR investigations and analysis of the multinuclear NMR data. Contribution to writing of the manuscript.

Pr. Dr. Gildas Gbassi, PhD supervisor, project management.

Dr. Patrick Atheba, general supervision of the experimental tasks.

Dr. Mathieu Fregnaux, XPS and Raman studies, contribution to the writing of the manuscript.

Jordi Buils, PhD student, computational calculations such as electronic structure studies and IR, Raman and NMR calculations and contribution to the writing of the manuscript.

Dr. Mireia Segado-Centellas, supervision of the computational tasks.

Pr. Dr. Carles Bo, writing of the manuscript and project management (lead).

Pr. Dr. Emmanuel Cadot, writing of the manuscript and project management (lead).

ACKNOWLEDGMENTS

This work is supported by a public grant overseen by the French National Research Agency as part of the "Investissements d'Avenir" program (Labex Charm3at, ANR-11-LABX-0039-grat), and by the Paris Ile-de-France region-DIM "Respore". The Ivory Coast Government is acknowledged for the F-I-B doctoral grant. The CNRS (France) and the University of Versailles Saint Quentin (UVSQ, France) are also acknowledged for financial support.

We acknowledge the Spanish Ministry of Science, Innovation and Universities MCIN/AEI/10.13039/501100011033 (PID2020-112806RB-I00 and CEX2019-000925-S), the ICIQ Foundation and the CERCA program of the Generalitat de Catalunya for funding.

REFERENCES

(1) Pope, M. T. *Heteropoly and Isopoly Oxometalates*; Springer-Verlag Berlin and Heidelberg: Berlin, Germany, 1983.

(2) Pope, M. T.; Müller, A. Polyoxometalate Chemistry: An Old Field with New Dimensions in Several Disciplines. *Angew. Chem. Int. Ed.* **1991**, *30* (1), 34–48. https://doi.org/10.1002/anie.199100341.

(3) Gumerova, N. I.; Rompel, A. Polyoxometalates in Solution: Speciation under Spotlight. *Chem. Soc. Rev.* **2020**, *49* (21), 7568–7601. https://doi.org/10.1039/D0CS00392A.

(4) Launay, J. P. Réduction de l'ion métatungstate: Stade élevé de réduction de $[H_2W_{12}O_{40}]^{6-}$, dérivé de $[HW_{12}O_{40}]^{7-}$ et discussion générale. *C. R. Acad. Sci*. **1969**, 971.

(5) Chen, J.-J.; Symes, M. D.; Cronin, L. Highly Reduced and Protonated Aqueous Solutions of $[P_2W_{18}O_{62}]^{6-}$ for on-Demand Hydrogen Generation and Energy Storage. *Nature Chem* **2018**, *10* (10), 1042–1047. https://doi.org/10.1038/s41557-018-0109-5.

(6) Wang, H.; Hamanaka, S.; Nishimoto, Y.; Irle, S.; Yokoyama, T.; Yoshikawa, H.; Awaga, K. In Operando X-Ray Absorption Fine Structure Studies of Polyoxometalate Molecular Cluster Batteries: Polyoxometalates as Electron Sponges. *J. Am. Chem. Soc.* **2012**, *134* (10), 4918–4924. https://doi.org/10.1021/ja2117206.

(7) Lee, J.-S.; Lee, C.; Lee, J.-Y.; Ryu, J.; Ryu, W.-H. Polyoxometalate as a Nature-Inspired Bifunctional Catalyst for Lithium–Oxygen Batteries. *ACS Catal.* **2018**, *8* (8), 7213–7221. https://doi.org/10.1021/acscatal.8b01103.

(8) Robin, M. B.; Day, P. Mixed Valence Chemistry-A Survey and Classification. In *Advances in Inorganic Chemistry and Radiochemistry*; Emeléus, H. J., Sharpe, A. G., Eds.; Academic Press, 1968; Vol. 10, pp 247–422. https://doi.org/10.1016/S0065-2792(08)60179-X.
(9) Jordan, J. W.; Lowe, G. A.; McSweeney, R. L.; Stoppiello, C. T.; Lodge, R. W.; Skowron, S. T.; Biskupek, J.; Rance, G. A.; Kaiser, U.; Walsh, D. A.; Newton, G. N.; Khlobystov, A. N. Host–Guest Hybrid Redox Materials Self-Assembled from Polyoxometalates and Single-Walled Carbon Nanotubes. *Adv. Mat.* **2019**, *31* (41), 1904182. https://doi.org/10.1002/adma.201904182.
(10) Hu, J.; Diao, H.; Luo, W.; Song, Y.-F. Dawson-Type Polyoxomolybdate Anions ($P_2Mo_{18}O_{62}^{6-}$) Captured by Ionic Liquid on Graphene Oxide as High-Capacity Anode Material for Lithium-Ion Batteries. *Chem.–Eur. J.* **2017**, *23* (36), 8729–8735. https://doi.org/10.1002/chem.201701121.
(11) Xiao, C.; Zhang, L.; Wang, K.; Wang, H.; Zhou, Y.; Wang, W. A New Approach to Enhance Photocatalytic Nitrogen Fixation Performance via Phosphate-Bridge: A Case Study of SiW12/K-C3N4. *Appl. Catal. B: Environmental* **2018**, *239*, 260–267. https://doi.org/10.1016/j.apcatb.2018.08.012.
(12) Zhou, X.; Yu, H.; Zhao, D.; Wang, X.; Zheng, S. Combination of Polyoxotantalate and Metal Sulfide: A New-Type Noble-Metal-Free Binary Photocatalyst $Na_8Ta_6O_{19}/Cd_{0.7}Zn_{0.3}S$ for Highly Efficient Visible-Light-Driven H_2 Evolution. *Appl. Catal. B: Environmental* **2019**, *248*, 423–429. https://doi.org/10.1016/j.apcatb.2019.02.052.
(13) Simms, C.; Kondinski, A.; Parac-Vogt, T. N. Metal-Addenda Substitution in Plenary Polyoxometalates and in Their Modular Transition Metal Analogues. *Eur. J. Inorg. Chem.* **2020**, *2020* (27), 2559–2572. https://doi.org/10.1002/ejic.202000254.
(14) Lv, H.; Guo, W.; Wu, K.; Chen, Z.; Bacsa, J.; Musaev, D. G.; Geletii, Y. V.; Lauinger, S. M.; Lian, T.; Hill, C. L. A Noble-Metal-Free, Tetra-Nickel Polyoxotungstate Catalyst for Efficient Photocatalytic Hydrogen Evolution. *J. Am. Chem. Soc.* **2014**, *136* (40), 14015–14018. https://doi.org/10.1021/ja5084078.
(15) Tourneur, J.; Fabre, B.; Loget, G.; Vacher, A.; Mériadec, C.; Ababou-Girard, S.; Gouttefangeas, F.; Joanny, L.; Cadot, E.; Haouas, M.; Leclerc-Laronze, N.; Falaise, C.; Guillon, E. Molecular and Material Engineering of Photocathodes Derivatized with Polyoxometalate-Supported {Mo3S4} HER Catalysts. *J. Am. Chem. Soc.* **2019**, *141* (30), 11954–11962. https://doi.org/10.1021/jacs.9b03950.
(16) Benseghir, Y.; Solé-Daura, A.; Mialane, P.; Marrot, J.; Dalecky, L.; Béchu, S.; Frégnaux, M.; Gomez-Mingot, M.; Fontecave, M.; Mellot-Draznieks, C.; Dolbecq, A. Understanding the Photocatalytic Reduction of CO2 with Heterometallic Molybdenum(V) Phosphate Polyoxometalates in Aqueous Media. *ACS Catal.* **2022**, *12* (1), 453–464. https://doi.org/10.1021/acscatal.1c04530.
(17) Nagaiah, T. C.; Gupta, D.; Adhikary, S. D.; Kafle, A.; Mandal, D. Tuning Polyoxometalate Composites with Carbonaceous Materials towards Oxygen Bifunctional Activity. *J. Mater. Chem. A* **2021**, *9* (14), 9228–9237. https://doi.org/10.1039/D0TA10423J.
(18) Li, X.-H.; He, P.; Wang, T.; Zhang, X.-W.; Chen, W.-L.; Li, Y.-G. Keggin-Type Polyoxometalate-Based ZIF-67 for Enhanced Photocatalytic Nitrogen Fixation. *ChemSusChem* **2020**, *13* (10), 2769–2778. https://doi.org/10.1002/cssc.202000328.
(19) Bonchio, M.; Syrgiannis, Z.; Burian, M.; Marino, N.; Pizzolato, E.; Dirian, K.; Rigodanza, F.; Volpato, G. A.; La Ganga, G.; Demitri, N.; Berardi, S.; Amenitsch, H.; Guldi, D. M.; Caramori, S.; Bignozzi, C. A.; Sartorel, A.; Prato, M. Hierarchical Organization of Perylene

Bisimides and Polyoxometalates for Photo-Assisted Water Oxidation. *Nat. Chem.* **2019**, *11* (2), 146–153. https://doi.org/10.1038/s41557-018-0172-y.
(20) Toma, F. M.; Sartorel, A.; Iurlo, M.; Carraro, M.; Parisse, P.; Maccato, C.; Rapino, S.; Gonzalez, B. R.; Amenitsch, H.; Da Ros, T.; Casalis, L.; Goldoni, A.; Marcaccio, M.; Scorrano, G.; Scoles, G.; Paolucci, F.; Prato, M.; Bonchio, M. Efficient Water Oxidation at Carbon Nanotube–Polyoxometalate Electrocatalytic Interfaces. *Nat. Chem.* **2010**, *2* (10), 826–831. https://doi.org/10.1038/nchem.761.
(21) Zhong, J.; Pérez-Ramírez, J.; Yan, N. Biomass Valorisation over Polyoxometalate-Based Catalysts. *Green Chem.* **2021**, *23* (1), 18–36. https://doi.org/10.1039/D0GC03190A.
(22) Zha, B.; Li, C.; Li, J. Efficient Electrochemical Reduction of CO2 into Formate and Acetate in Polyoxometalate Catholyte with Indium Catalyst. *J. Catal.* **2020**, *382*, 69–76. https://doi.org/10.1016/j.jcat.2019.12.010.
(23) Meyer, R. L.; Anjass, M. H.; Petel, B. E.; Brennessel, W. W.; Streb, C.; Matson, E. M. Electronic Consequences of Ligand Substitution at Heterometal Centers in Polyoxovanadium Clusters: Controlling the Redox Properties through Heterometal Coordination Number. *Chem.–Eur. J.* **2020**, *26* (44), 9905–9914. https://doi.org/10.1002/chem.201905624.
(24) Tommasino, J. B.; Contant, R.; Michaut, J. P.; Roncin, J. Electrochemical Characterization of a Series of Substituted Dawson Type Tungstophosphates $\alpha[P_2W_{18-x}Mo_zV_yO_{62}]^{n-}$ (x = y + z; n = 6 + y). *Polyhedron* **1998**, *17* (2), 357–366. https://doi.org/10.1016/S0277-5387(97)00274-X.
(25) Cadot, E.; Thouvenot, R.; Teze, A.; Herve, G. Syntheses and Multinuclear NMR Characterizations of α-$[SiMo_2W_9O_{39}]^{8-}$ and .Alpha.-$[SiMo_{3-x}V_xW_9O_{40}]^{(4+x)-}$ (x = 1, 2) Heteropolyoxometalates. *Inorg. Chem.* **1992**, *31* (20), 4128–4133. https://doi.org/10.1021/ic00046a026.
(26) Abbessi, M.; Contant, R.; Thouvenot, R.; Herve, G. Dawson Type Heteropolyanions. 1. Multinuclear (Phosphorus-31, Vanadium-51, Tungsten-183) NMR Structural Investigations of Octadeca(Molybdotungstovanado)Diphosphates α-1,2,3-$[P_2MM'_2W_{15}O_{62}]^{n-}$ (M, M' = Mo, V, W): Syntheses of New Related Compounds. *Inorg. Chem.* **1991**, *30* (8), 1695–1702. https://doi.org/10.1021/ic00008a006.
(27) Contant, R.; Abbessi, M.; Thouvenot, R.; Hervé, G. Dawson Type Heteropolyanions. 3. Syntheses and 31P, 51V, and 183W NMR Structural Investigation of Octadeca(Molybdo−tungsto−vanado)Diphosphates Related to the $[H_2P_2W_{12}O_{48}]^{12-}$ Anion. *Inorg. Chem.* **2004**, *43* (12), 3597–3604. https://doi.org/10.1021/ic049885w.
(28) Jeannin, Y.; Martin-Frere, J. Tungsten-183 NMR and x-Ray Study of a Heteropolyanion $[As_2W_{21}O_{69}(H_2O)]^{6-}$ Exhibiting a Rare Square-Pyramidal Environment for Some Tungsten(VI). *J. Am. Chem. Soc.* **1981**, *103* (7), 1664–1667. https://doi.org/10.1021/ja00397a012.
(29) Robert, F.; Leyrie, M.; Herve, G.; Teze, A.; Jeannin, Y. Crystal-Structure of Ammonium Dicobalto(Ii)-40-Tungstotetraarsenate(III) - Allosteric Effects in the Ligand. *Inorg. Chem.* **1980**, *19* (6), 1746–1752. https://doi.org/10.1021/ic50208a065.
(30) Leyrie, M.; Thouvenot, R.; Teze, A.; Herve, G. Polyoxotungstates with Lone-Pair Assembling Atoms .1. Alkali and Alkaline-Earth Cryptates of the $[Co_2(H_2O)_2\ As_4W_{40}O_{140}]^{24-}$ Inorganic Complex - Interaction Between the Metal Centers. *New J. Chem.* **1992**, *16* (4), 475–481.
(31) Kortz, U.; Savelieff, M. G.; Bassil, B. S.; Dickman, M. H. A Large, Novel Polyoxotungstate: $[As_6W_{65}O_{217}(H_2O)_7]^{26-}$. *Angew. Chem. Int. Ed.* **2001**, *40* (18), 3384–3386.

https://doi.org/10.1002/1521-3773(20010917)40:18<3384::AID-ANIE3384>3.0.CO;2-O.
(32) Lefebvre, F.; Leyrie, M.; Herve, G.; Sanchez, C.; Livage, J. Square Pyramidal Complexes of Divalent Cations of the First Transition Row with the 20-Tungsto-2-Arsenate(III): Synthesis, Visible and E.S.R. Spectra. *Inorg. Chim. Acta* **1983**, *73*, 173–178. https://doi.org/10.1016/S0020-1693(00)90847-8.
(33) Lin, Z.; Izarova, N. V.; Mehari, F. T.; Kortz, U. Palladium(II) Incorporation in the All-Inorganic Cryptand $[As_4W_{40}O_{140}]^{28-}$: Synthesis and Structural Characterization of $[Pd_2Na_2KAs_4W_{40}O_{140}(H_2O)]^{21-}$. *Z. anorg. all Chem.* **2018**, *644* (22), 1379–1382. https://doi.org/10.1002/zaac.201800327.
(34) Bamba, I. F.; Falaise, C.; Marrot, J.; Gbassi, G. K.; Atheba, P.; Guillot, R.; Haouas, M.; Cadot, E. Revisiting the Three Vanadium Sandwich-Type Polyoxometalates: Structures, Solution Behavior, and Redox Properties. *Inorg. Chem.* **2022**, *61* (21), 8309–8319. https://doi.org/10.1021/acs.inorgchem.2c00776.
(35) Leparulo-Loftus, M. A.; Pope, M. T. Vanadium-51 NMR Spectroscopy of Tungstovanadate Polyanions. Chemical Shift and Line-Width Patterns for the Identification of Stereoisomers. *Inorg. Chem.* **1987**, *26* (13), 2112–2120. https://doi.org/10.1021/ic00260a021.
(36) Domaille, P. J.; Watunya, G. Synthesis and Tungsten-183 NMR Characterization of Vanadium-Substituted Polyoxometalates Based on B-Type Tungstophosphate $PW_9O_{34}^{9-}$ Precursors. *Inorg. Chem.* **1986**, *25* (8), 1239–1242. https://doi.org/10.1021/ic00228a033.
(37) Jeannin, Y. P. The Nomenclature of Polyoxometalates: How To Connect a Name and a Structure. *Chem. Rev.* **1998**, *98* (1), 51–76. https://doi.org/10.1021/cr960397i.
(38) Sundaram, K. M.; Neiwert, W. A.; Hill, C. L.; Weinstock, I. A. Relative Energies of α and β Isomers of Keggin Dodecatungstogallate. *Inorg. Chem.* **2006**, *45* (3), 958–960. https://doi.org/10.1021/ic051789n.
(39) Tanuma, S.; Powell, C. J.; Penn, D. R. Calculations of Electron Inelastic Mean Free Paths. V. Data for 14 Organic Compounds over the 50–2000 eV Range. *Surf. Int. An.* **1994**, *21* (3), 165–176. https://doi.org/10.1002/sia.740210302.
(40) Shinotsuka, H.; Tanuma, S.; Powell, C. J.; Penn, D. R. Calculations of Electron Inelastic Mean Free Paths. X. Data for 41 Elemental Solids over the 50 eV to 200 keV Range with the Relativistic Full Penn Algorithm. *Surf. Int. An.* **2015**, *47* (9), 871–888. https://doi.org/10.1002/sia.5789.
(41) Mizokawa, Y.; Iwasaki, H.; Nishitani, R.; Nakamura, S. Esca Studies of Ga, As, GaAs, Ga2O3, As2O3 and As2O5. *J. Elect. Spect. Rel. Phenom.* **1978**, *14* (2), 129–141. https://doi.org/10.1016/0368-2048(78)85061-0.
(42) Rei Vilar, M.; El Beghdadi, J.; Debontridder, F.; Artzi, R.; Naaman, R.; Ferraria, A. M.; Botelho do Rego, A. M. Characterization of Wet-Etched GaAs (100) Surfaces. *Surf. Int. An.* **2005**, *37* (8), 673–682. https://doi.org/10.1002/sia.2062.
(43) Altenau, J. J.; Pope, M. T.; Prados, R. A.; So, Hyunsoo. Models for Heteropoly Blues. Degrees of Valence Trapping in Vanadium(IV)- and Molybdenum(V)-Substituted Keggin Anions. *Inorg. Chem.* **1975**, *14* (2), 417–421. https://doi.org/10.1021/ic50144a042.
(44) Mossoba, M. M.; O'Connor, C. J.; Pope, M. T.; Sinn, E.; Herve, G.; Teze, A. Mixed Valence and Magnetically Coupled Vanadate Domains in Heteropoly Tungstate Anions. *J. Am. Chem. Soc.* **1980**, *102* (22), 6864–6866. https://doi.org/10.1021/ja00542a042.
(45) Harmalker, S. P.; Leparulo, M. A.; Pope, M. T. Mixed-Valence Chemistry of Adjacent Vanadium Centers in Heteropolytungstate Anions. I. Synthesis and Electronic Structures of Mono-, Di-, and Trisubstituted Derivatives of .Alpha.-Octadecatungstodiphosphate(6-) Ion

(α-$[P_2W_{18}O_{62}]^{6-}$). *J. Am. Chem. Soc.* **1983**, *105* (13), 4286–4292. https://doi.org/10.1021/ja00351a028.
(46) Ballhausen, C. J.; Gray, H. B. The Electronic Structure of the Vanadyl Ion. *Inorg. Chem.* **1962**, *1* (1), 111–122. https://doi.org/10.1021/ic50001a022.
(47) Son, J.-H.; Casey, W. H. Reversible Capping/Uncapping of Phosphorous-Centered Keggin-Type Polyoxoniobate Clusters. *Chem. Commun.* **2015**, *51* (8), 1436–1438. https://doi.org/10.1039/C4CC05689B.
(48) Shmakova, A. A.; Abramov, P. A.; Sokolov, M. N. Synthesis, Stability, and Crystal Structure of the $(NMe_2H_2)_9[(AsW_9O_{33})_2(NbO)_3(H_2O)]\cdot 44H_2O$ Complex. *J. Struct. Chem.* **2019**, *60* (4), 623–629. https://doi.org/10.1134/S0022476619040139.
(49) Dolomanov, O. V., Bourhis, L. J., Gildea, R. J., Howard, J. a. K. & Puschmann, H. OLEX2: a complete structure solution, refinement and analysis program. *J. Appl. Crystallogr.* **2009,** *42,* 339–34. https://doi.org/10.1107/S0021889808042726.
(50) Sheldrick, G. M. SHELXT – Integrated space-group and crystal-structure determination. *Acta Crystallogr. Sect. Found. Adv.* **2015**, *71*, 3–8. https://doi.org/10.1107/S2053273314026370.
(51) Te Velde, G., Bickelhaupt, F. M., Baerends, E. J., Fonseca Guerra, C., Van Gisbergen, S. J. A., Snijders, J. G.; Ziegler, T. Chemistry with ADF. *J. Comput. Chem.* **2001**, *22* (9), 931–967. https://doi.org/10.1002/jcc.1056.
(52) Becke, A. D. Density-Functional Exchange-Energy Approximation with Correct Asymptotic Behavior. *Phys. Rev. A* **1988***, **38*** (6), 3098–3100. https://doi.org/10.1103/PhysRevA.38.3098.
(53) Perdew, J. P. Density-Functional Approximation for the Correlation Energy of the Inhomogeneous Electron Gas. P*hys. Rev. B* **1986**, *33* (12), 8822–8824. https://doi.org/10.1103/PhysRevB.33.8822.
(54) Van Lenthe, E., Baerends, E. J. Optimized Slater-type Basis Sets for the Elements 1–118. *J. Comput. Chem.* **2003***, 24* (9), 1142–1156. https://doi.org/10.1002/jcc.10255.
(55) Lenthe, E. V., Baerends, E. J.; Snijders, J. G. Relativistic Regular Two-Component Hamiltonians. *J. Chem. Phys.* **1993***, 99* (6), 4597–4610. https://doi.org/10.1063/1.466059.
(56) Klamt, A. Conductor-like Screening Model for Real Solvents: A New Approach to the Quantitative Calculation of Solvation Phenomena. *J. Phys. Chem.***1995***, 99* (7), 2224–2235. https://doi.org/10.1021/j100007a062.
(57) Autschbach, J., Ziegler, T. Nuclear Spin–Spin Coupling Constants from Regular Approximate Relativistic Density Functional Calculations. II. Spin–Orbit Coupling Effects and Anisotropies. *J. Chem. Phys.* **2000***, 113* (21), 9410–9418. https://doi.org/10.1063/1.1321310.
(58) Autschbach, J., Ziegler, T. Nuclear Spin–Spin Coupling Constants from Regular Approximate Relativistic Density Functional Calculations. I. Formalism and Scalar Relativistic Results for Heavy Metal Compounds. *J. Chem. Phys.* **2000***, 113* (3), 936–947. https://doi.org/10.1063/1.481874.
(59) Schreckenbach, G., Ziegler, T. Calculation of NMR Shielding Tensors Using Gauge-Including Atomic Orbitals and Modern Density Functional Theory. *J. Phys. Chem.* **1995***, 99* (2), 606–611. https://doi.org/10.1021/j100002a024.
(60) Swart, M.; Ehlers, A. W.; Lammertsma, K. Performance of the OPBE Exchange-Correlation Functional. *Mol. Phys.* **2004***, 102* (23-24), 2467–2474. https://doi.org/10.1080/00268970420002750 17.

(61) Álvarez-Moreno, M., De Graaf, C., López, N., Maseras, F., Poblet, J. M., Bo, C. Managing the Computational Chemistry Big Data Problem: The ioChem-BD Platform. *J. Chem. Inf. Model.* **2015***, 55* (1), 95–103. https://doi.org/10.1021/ci500593j.
(62) Robert, F., Leyrie, M. & Hervé, G. Structure of potassium diaquatricuprooctadecatungstodiarsenate(III)(12–) undecahydrate. *Acta Crystallogr. B* **1982**, *38*, 358–362. https://doi.org/10.1107/s0567740882002970.
(63) Tourne, C. & Tourne, G. 19-Tungstodimetallo-Diarsenates 3 Preliminary Study. *C. R. Acad. Sci. Ser. C* **1975***, 281* (22), 933–936.
(64) Contant, R., Thouvenot, R., Dromzée, Y., Proust, A. & Gouzerh, P. Synthesis and Structural Chemistry of Tungstoarsenates(V). *J. Clust. Sci.* **2006***, 17* (2), 317–33. https://doi.org/10.1007/s10876-006-0054-0.

TOC